

Charge carrier transport in defective reduced graphene oxide as quantum dots and nanoplatelets in multilayer films

Jimenez, Mawin J.M.; Oliveira, Rafael F.; Pedroso de Almeida, T.; Ferreira, Rafael C.Hensel; Bufon, Carlos Cesar B.; Rodrigues, Varlei; Pereira-Da-Silva, Marcelo A.; Gobbi, Angelo L.; Piazzetta, Maria H.O.; Riul, Antonio

DOI

[10.1088/1361-6528/aa91c2](https://doi.org/10.1088/1361-6528/aa91c2)

Publication date

2017

Document Version

Final published version

Published in

Nanotechnology

Citation (APA)

Jimenez, M. J. M., Oliveira, R. F., Pedroso de Almeida, T., Ferreira, R. C. H., Bufon, C. C. B., Rodrigues, V., Pereira-Da-Silva, M. A., Gobbi, A. L., Piazzetta, M. H. O., & Riul, A. (2017). Charge carrier transport in defective reduced graphene oxide as quantum dots and nanoplatelets in multilayer films. *Nanotechnology*, 28(49), 1-11. Article 495711. <https://doi.org/10.1088/1361-6528/aa91c2>

Important note

To cite this publication, please use the final published version (if applicable).
Please check the document version above.

Copyright

Other than for strictly personal use, it is not permitted to download, forward or distribute the text or part of it, without the consent of the author(s) and/or copyright holder(s), unless the work is under an open content license such as Creative Commons.

Takedown policy

Please contact us and provide details if you believe this document breaches copyrights.
We will remove access to the work immediately and investigate your claim.

PAPER

Charge carrier transport in defective reduced graphene oxide as quantum dots and nanoplatelets in multilayer films

To cite this article: Mawin J M Jimenez *et al* 2017 *Nanotechnology* **28** 495711

View the [article online](#) for updates and enhancements.

Related content

- [Functional chemically modified graphene film: microstructure and electrical transport behavior](#)
Junsheng Ma, Xueyan Hou, Mingpeng Yu *et al*.
- [Nanoassemblies of sulfonated polyaniline multilayers](#)
Nabin Sarkar, Manoj Ku Ram, Anjana Sarkar *et al*.
- [Investigation of disorder and its effect on electrical transport in electrochemically doped polymer devices by current–voltage and impedance spectroscopy](#)
Motiur Rahman Khan, P Anjaneyulu, K S R Koteswara Rao *et al*.

Recent citations

- [Maria L. Braunger *et al*](#)
- [Enhanced mobility and controlled transparency in multilayered reduced graphene oxide quantum dots: a charge transport study](#)
Mawin J M Jimenez *et al*
- [Experimental and computational investigation of reduced graphene oxide nanoplatelets stabilized in poly\(styrene sulfonate\) sodium salt](#)
Celina M. Miyazaki *et al*



240th ECS Meeting ORLANDO, FL

Orange County Convention Center **Oct 10-14, 2021**

Abstract submission deadline extended: April 23rd

SUBMIT NOW

Charge carrier transport in defective reduced graphene oxide as quantum dots and nanoplatelets in multilayer films

Mawin J M Jimenez¹ , Rafael F Oliveira² , Tiago P Almeida^{3,4},
Rafael C Hensel Ferreira¹, Carlos Cesar B Bufon², Varlei Rodrigues¹,
Marcelo A Pereira-da-Silva^{5,6} , Ângelo L Gobbi², Maria H O Piazzetta² and
Antonio Riul Jr^{1,7} 

¹ Department of Applied Physics, ‘Gleb Wataghin’ Institute of Physics, University of Campinas—UNICAMP, 13083-970, Campinas, SP, Brazil

² Brazilian Nanotechnology National Laboratory (LNNano), Brazilian Center for Research in Energy and Materials (CNPEM), 13083-970, Campinas, SP, Brazil

³ PhD Program in Bionergy, University of Campinas, 13083-862, Campinas, SP, Brazil

⁴ Department of Biotechnology, Department of Biotechnology/Biocatalysis Delft University of Technology Van der Maasweg 9, 2629 HZ Delft, The Netherlands

⁵ Centro Universitário Central Paulista—UNICEP, 13563-470, São Carlos, SP, Brazil

⁶ Instituto de Física de São Carlos—IFSC/USP, 13560-250, São Carlos, SP, Brazil

E-mail: riul@ifi.unicamp.br

Received 2 August 2017, revised 3 October 2017

Accepted for publication 6 October 2017

Published 15 November 2017



CrossMark

Abstract

Graphene is a breakthrough 2D material due to its unique mechanical, electrical, and thermal properties, with considerable responsiveness in real applications. However, the coverage of large areas with pristine graphene is a challenge and graphene derivatives have been alternatively exploited to produce hybrid and composite materials that allow for new developments, considering also the handling of large areas using distinct methodologies. For electronic applications there is significant interest in the investigation of the electrical properties of graphene derivatives and related composites to determine whether the characteristic 2D charge transport of pristine graphene is preserved. Here, we report a systematic study of the charge transport mechanisms of reduced graphene oxide chemically functionalized with sodium polystyrene sulfonate (PSS), named as GPSS. GPSS was produced either as quantum dots (QDs) or nanoplatelets (NPLs), being further nanostructured with poly(diallyldimethylammonium chloride) through the layer-by-layer (LbL) assembly to produce graphene nanocomposites with molecular level control. Current–voltage (I – V) measurements indicated a meticulous growth of the LbL nanostructures onto gold interdigitated electrodes (IDEs), with a space-charge-limited current dominated by a Mott-variable range hopping mechanism. A 2D intra-planar conduction within the GPSS nanostructure was observed, which resulted in effective charge carrier mobility (μ) of $4.7 \text{ cm}^2 \text{ V}^{-1} \text{ s}^{-1}$ for the QDs and $34.7 \text{ cm}^2 \text{ V}^{-1} \text{ s}^{-1}$ for the NPLs. The LbL assemblies together with the dimension of the materials (QDs or NPLs) were favorably used for the fine tuning and control of the charge carrier mobility inside the LbL nanostructures. Such 2D charge conduction mechanism and high μ values inside an interlocked multilayered assembly containing graphene-based nanocomposites are of great interest for organic devices and functionalization of interfaces.

⁷ Author to whom any correspondence should be addressed.

Keywords: reduced graphene oxide, quantum dots, nanoplatelets, charge transport, layer-by-layer assembly, space-charge-limited current, variable-range hopping

(Some figures may appear in colour only in the online journal)

Introduction

Graphene has attracted great interest in the last decade due to its unique optical, electrical and mechanical properties [1–4], clearly evidenced by the increasing number of publications [5, 6]. Nevertheless, obtaining pristine graphene in large areas is a challenge even with recent progress in chemical vapor deposition methods that still require high temperatures (>300 °C) and expensive apparatus [7]. This naturally drives the search for new fabrication methodologies and hybrid or composite materials resembling the properties of pristine graphene. The layer-by-layer (LbL) technique is a simple, alternative approach for the functionalization of surfaces based on physical adsorption of materials. It is mainly based on hydrogen bonding, electrostatic and van der Waals interactions, allowing molecular level control in the assembly of graphene-based materials with other compounds for intricate functions [8–10]. The processing of materials is important for both the LbL assembly and other methodologies; and the chemical synthesis can be favorably used for both functionalization and production of water soluble hybrid, composite graphene-like compounds with properties that can be synergistically explored with other conjugated materials in a multitude of applications.

Reduced graphene oxide (rGO) is an attractive choice as it has properties resembling pristine graphene, although its electrical conductivity and charge carrier mobility are lower due to the presence of defects and remaining OH groups from the chemical reduction process [11]. rGO has been used in numerous technological applications such as flexible memories [12], sensors [13–15], supercapacitors [16] and batteries [17]. Research on the electrical characteristics of rGO suggests a space-charge-limited current (SCLC) conduction mechanism [18, 19] and temperature-dependent studies indicate charge carriers thermally activated by a variable-range hopping (VRH) process [20–22]. However, there is a lack of information in the literature about mobility, conductivity and charge carrier mechanisms in rGO nanostructures combined with other materials, especially as multilayered LbL films, which is important for forthcoming developments in electronic devices.

We report here a systematic study of the charge transport mechanisms of rGO chemically functionalized with sodium polystyrene sulfonate (PSS), named GPSS, either as quantum dots (QDs) or nanoplatelets (NPLs) in interlocked LbL nanostructures with poly(diallyldimethylammonium chloride) (PDDA). The materials were deposited onto gold interdigitated electrodes (IDEs) and electrical characterization was performed at each deposition step during the LbL film assembly, with charge transport dominated by the SCLC mechanism. The transit time of the charge carriers was determined from impedance measurements and, based on the SCLC formalism, used to define the mobility (μ) and density

of carriers thermally generated in the LbL nanostructures. The charge carrier conduction in both QDs and NPLs can be well described by the VRH Mott model (Mott-VRH), presenting a 2D intra-planar conduction formed within the GPSS plane in the LbL structure with almost null inter-planar passage between adjacent film layers. Interestingly, such multilayered LbL assemblies enable 3D nanostructures with controlled thickness and composition that preserve the characteristic 2D charge transport of graphene-based materials along with the layer where the QDs or NPLs are deposited.

Experimental

Graphene oxide (GO) was chemically synthesized from the traditional Hummers' method [23], yielding a black powder. Briefly, 250 mg of GO were sonicated for 10 min in ultrapure water acquired from a Sartorius Arium Comfort system, resulting in homogeneous, stable GO water suspension. The GO dispersion was added with 2.5 g of poly(sodium 4-styrenesulfonate) (PSS) acquired from Sigma-Aldrich under continuous stirring, followed by the addition of 325.5 mg of hydrazine at ~90 °C during 14 h, thus producing stable rGO wrapped by PSS molecules (GPSS) [24]. The final product was centrifuged at 1500 rpm, further washed with ultrapure water and then dried in vacuum. GPSS NPLs were obtained after diluting the material in ultrapure water (0.1 mg ml⁻¹), keeping the dispersion in an ultrasonic bath for ~30 min. GPSS in QDs form were prepared by immersing an ultrasonic probe (QSonica Sonicators model Q700) in the GPSS solution for 30 min.

For the LbL film formation, GPSS was used as the negatively charged polyelectrolyte prepared in ultrapure water at 0.1 g l⁻¹. Poly(diallyldimethylammonium chloride) (PDDA) acquired from Sigma-Aldrich was used as received and employed as the positively charged polyelectrolyte at 20 wt% in ultrapure water. The pH of all polyelectrolytes was adjusted to 3.5 using 0.1 mol l⁻¹ HCl. LbL films were deposited onto gold IDEs having 60 fingers with 150 nm height, 3 mm length and 40 μ m width, separated 40 μ m each other, patterned onto glass slides by standard photolithography. The immersion time in both polyelectrolytes was fixed in 10 min, thus producing (PDDA/GPSS:QDs)_n and (PDDA/GPSS:NPLs)_n LbL films, being *n* the number of deposited bilayers. A washing step consisting of 1 s in ultrapure water also at pH 3.5 was adopted between sequential immersions into the polyelectrolytes to remove material loosely bonded. The multilayer formation was monitored at each deposition step by both UV–vis spectroscopy (Biochrom Libra S60 spectrometer) for LbL films deposited onto quartz plates, and through current (*I*) versus voltage (*V*) measurements for films deposited onto IDEs. The *I*–*V* data was acquired in a home-made automated setup controlled by

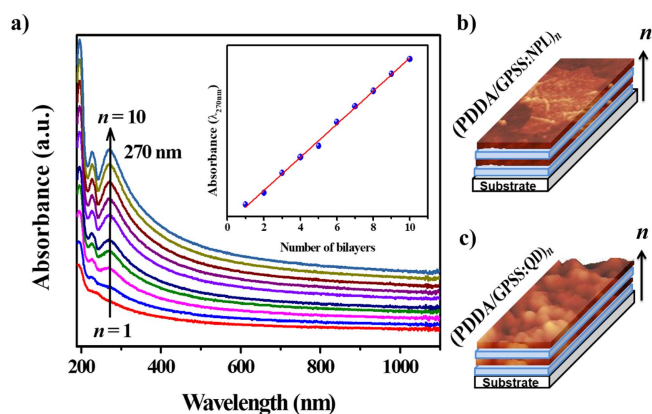


Figure 1. (a) LbL film growth of $(\text{PDDA}/\text{GPSS}:\text{QDs})_{10}$ monitored by UV-vis spectroscopy. Inset: film absorbance at 270 nm as a function of the number (n) of deposited bilayers, with the same behavior observed for $(\text{PDDA}/\text{GPSS}:\text{NPLs})_{10}$ LbL films. (b) and (c) Sketches of the $(\text{PDDA}/\text{GPSS}:\text{NPLs})_n$ and $(\text{PDDA}/\text{GPSS}:\text{QDs})_n$ film architectures, using their respective morphologies obtained from AFM measurements.

Arduino using a Keithley 6487 Picoammeter. A set of five I - V curves were obtained after withdrawal of the substrates from the rinsing water to check the stability of the electrical response. Atomic force microscopy (AFM) was carried out on a BRUKER Dimension ICON equipment with a rectangular shaped silicon tip, 42 N m^{-1} spring constant, 330 kHz free oscillation, in the intermittent contact mode. Impedance measurements were acquired using a Solarton 1260A impedance analyzer coupled to a 1296 dielectric interface. Measurements were carried out with sine-wave voltage signal amplitude of 25 mV, without dc bias in the frequency range 1 Hz–1 MHz at room temperature. To evaluate the charge transport mechanisms of the LbL films, I - V measurements as a function of temperature were carried out using a Keithley 2636A SourceMeter[®] coupled to an LTS420E Linkam cryostat in a probe station. The measurements were performed in vacuum (10^{-2} Torr) with the temperature varying from 77 to 327 K. Finally, carrier concentration, conductivity and Hall mobility measurements were performed at room temperature using an Ecopia HMS-3000 Hall System from Bridge Technology, operating in van der Pauw configuration and magnetic flux density input of 0.55 T.

Results and discussion

GPSS either as QDs or NPLs could be successfully tailored in a multilayered assembly with PDDA, as illustrated in figure 1 by the UV-vis spectra for QDs. The same behavior was observed for the GPSS NPL films, with results not shown as no additional information is added. It was observed a linear growth with the number of deposited bilayers from the absorbance maximum formed at 270 nm, commonly attributed to $\pi \rightarrow \pi^*$ transitions of aromatic C-C bonds in the graphitic structure [25, 26]. The observed linearity (figure 1 inset) is an indicative that the same amount of material was transferred at each deposition step in the $(\text{PDDA}/\text{GPSS})_n$

LbL film formation, with high degree of molecular organization and thickness control at nanoscale [27].

The AFM characterization of the LbL films confirms the presence of both NPLs (figure 2(a)) and QDs (figure 2(b)), as expected following the experimental procedure adopted for the GPSS solution preparation. From figure 2(a) one can notice the presence of both single and multiple stacked NPLs, with a root mean square (rms) roughness of 1.2 nm and average NPL diameter size ranging from 0.5 to $1.5 \mu\text{m}$, compatible to values reported in the literature [24, 28]. It was also identified the presence of wrinkled NPLs, with higher surface area than the QDs. The QDs (figure 2(b)) presented a uniform globular film characteristic with size ranging from 20 to 65 nm in diameter and average rms roughness of 6.4 nm, similar to literature [29–31]. From figure 2 it can be noticed the presence of wrinkled NPLs as single foils with average thickness of $\sim 1.59 \text{ nm}$, and also 18.8 nm as the average height of the QDs.

As the $(\text{PDDA}/\text{GPSS})_n$ film growth and topographies have been identified, electrical measurements were carried out during each deposition step in the LbL architectures, as shown in figure 3. The electric current measured in the QDs LbL films presented a strong dependence on the number of deposited bilayers (figure 3(a)). For the first 10 bilayers, the current minimum value is symmetrically reached for potentials other than 0 V in both positive and negative applied bias (figure 3(b)), a characteristic hysteretic effect indicative of trapped charges within the film [32]. With increasing number of deposited QDs bilayers the current continues to increase, with a concomitant decrease in the distance between the minimum values, indicative that the system is becoming more conductive and loses the capacity to store charges. This effect is highlighted in figure 3(a) where one can observe that up to the 20th deposited bilayer the current grows rapidly, with subsequent little current variations occurring from the 40th to the 50th bilayers. Such a behavior was observed in three independent samples, reaching $\sim 10^{-4} \text{ A}$ at 2 V. For LbL films with GPSS NPLs the same current values (10^{-4} A) were attained at lower voltages ($\sim 1 \text{ V}$) already for the 5th deposited bilayer, with no indications of charge trapping/accumulation (figure 3(c)). Details on the thickness-dependent current of each film are discussed hereafter. It is worth mentioning that the sp^2 large domains formed in the rGO NPLs are responsible for the observed high currents [33]; LbL films formed with QDs, on the other hand, present smaller sp^2 domains in larger disordered regions when compared with the NPLs. Smaller domains lead to an increased number of grain boundaries and interfaces that increase scattering during the charge transport, reducing the observed current [33]. Consequently, the LbL technique enables a fine tuning of the electrical properties that can be explored through surface modification of interfaces using distinct molecular assemblies of the same material.

Electrical dc and ac measurements were combined in a further insight into the charge transport of the LbL films. The range of the applied potential in dc measurements was increased beyond the ohmic region to check the validity of Schottky, Poole-Frenkel, Fowler-Nordheim, and SCLC

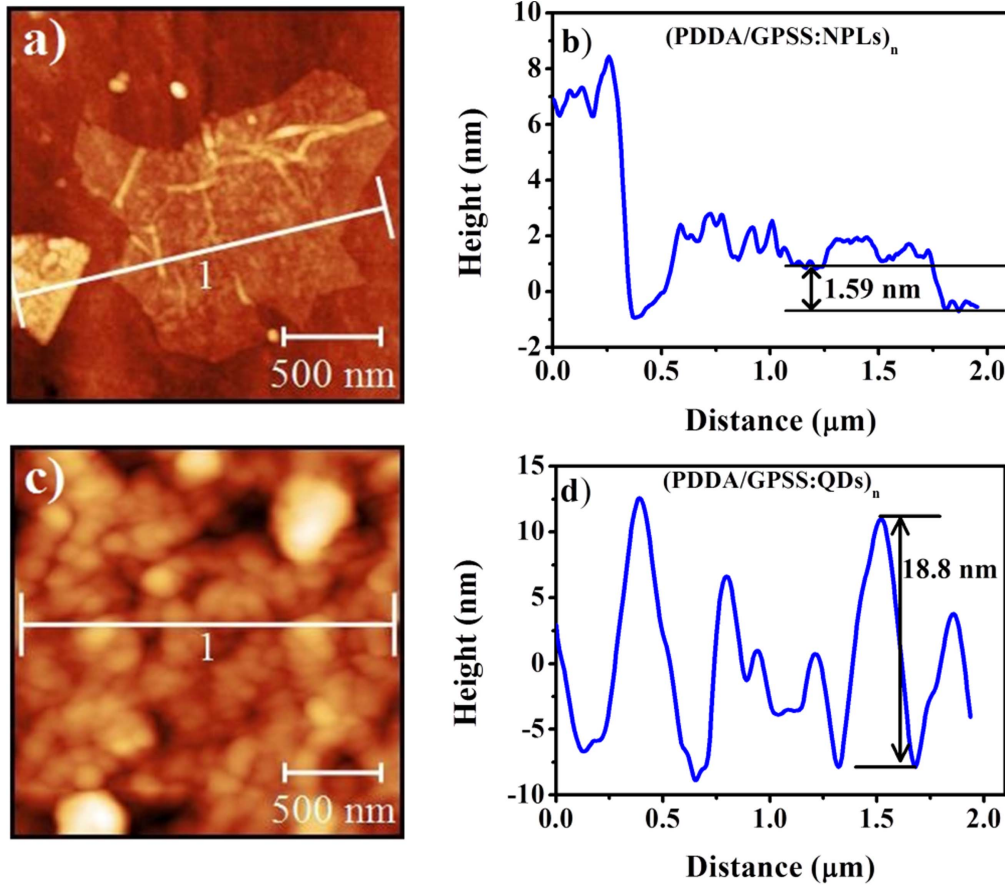


Figure 2. AFM image (a,c) of the LbL film and height profile (b,d) along the indicated line 1 for (PDDA/GPSS:NPLs)₅₀ and for (PDDA/GPSS:QDs)₅₀, respectively.

models [34–37]. Impedance measurements were used to determine the relaxation time of the charge carriers in the LbL films studied. The results are displayed in figure 4 for LbL films containing QDs and NPLs.

From figures 4(a), (c) one can observe an ohmic region (slope ~ 1) at low potentials, followed by a $I \propto V^n$ dependence with $n = 2$ for higher voltages, characteristic of the SCLC mechanism. The current density (J) in the ohmic region is given by equation (1):

$$J_{\Omega} = qn_0\mu\frac{V}{d}, \quad (1)$$

where q is the elementary charge, n_0 is the concentration of free charge carriers in thermal equilibrium, μ the mobility of the charge carriers and d the distance between fingers in the IDEs. A parallel-plate capacitor approximation ($E = V/d$) can be used to describe the electric field (E) with respect to the applied voltage. For a semiconductor/insulator material in the presence of charged traps, the current densities in the SCLC regime are given by equation (2):

$$J = \frac{9}{8}\varepsilon_r\varepsilon_0\mu\theta\frac{V^2}{d^3}, \quad (2)$$

where ε_r is the relative permittivity of the material ($\varepsilon_r \sim 5$ for rGO according to the literature [18]), ε_0 is the vacuum permittivity ($8.85 \times 10^{-12} \text{ F m}^{-1}$), θ is the ratio between the

density of free carriers and the total density of carriers (viz. free and trapped charges).

The transition from ohmic to SCLC conduction occurs in a characteristic potential called transition voltage (V_{Ω}), as indicated in figures 4(a), (c) for the films containing QDs and NPLs, respectively. At this condition, the transit time of the carriers $t_t = d^2/(\mu\theta V_{\Omega})$ is approximately equal to the dielectric relaxation time $\tau = (9\varepsilon_r\varepsilon_0)/(8qn_0\mu)$ [35, 38–40], which gives equation (3) for V_{Ω} [39]:

$$V_{\Omega} = \frac{8}{9}\frac{qn_0d^2}{\theta\varepsilon_r\varepsilon_0}. \quad (3)$$

The transition voltage can be obtained from the I - V plot, as indicated in figures 4(a), (c), being respectively 0.85 V for the (PDDA/GPSS:QDs)₅₀ and 2.9 V for the (PDDA/GPSS:NPLs)₅₀ films.

The dielectric relaxation time (τ) was determined from the impedance data, represented here as Nyquist plots ($-Z''$ versus Z'), as shown in figures 4(b), (d). The semicircle formed with its maximum at the frequency $\omega_{\max} = 2\pi f_{\max}$ provides $\tau = 1/\omega_{\max}$ for the analyzed LbL film. The values are shown in table 1, along with other parameters calculated from the SCLC model.

The effective mobility (μ_{eff}) of the charge carriers indicated in table 1 were calculated considering $t_t \approx \tau$ at the

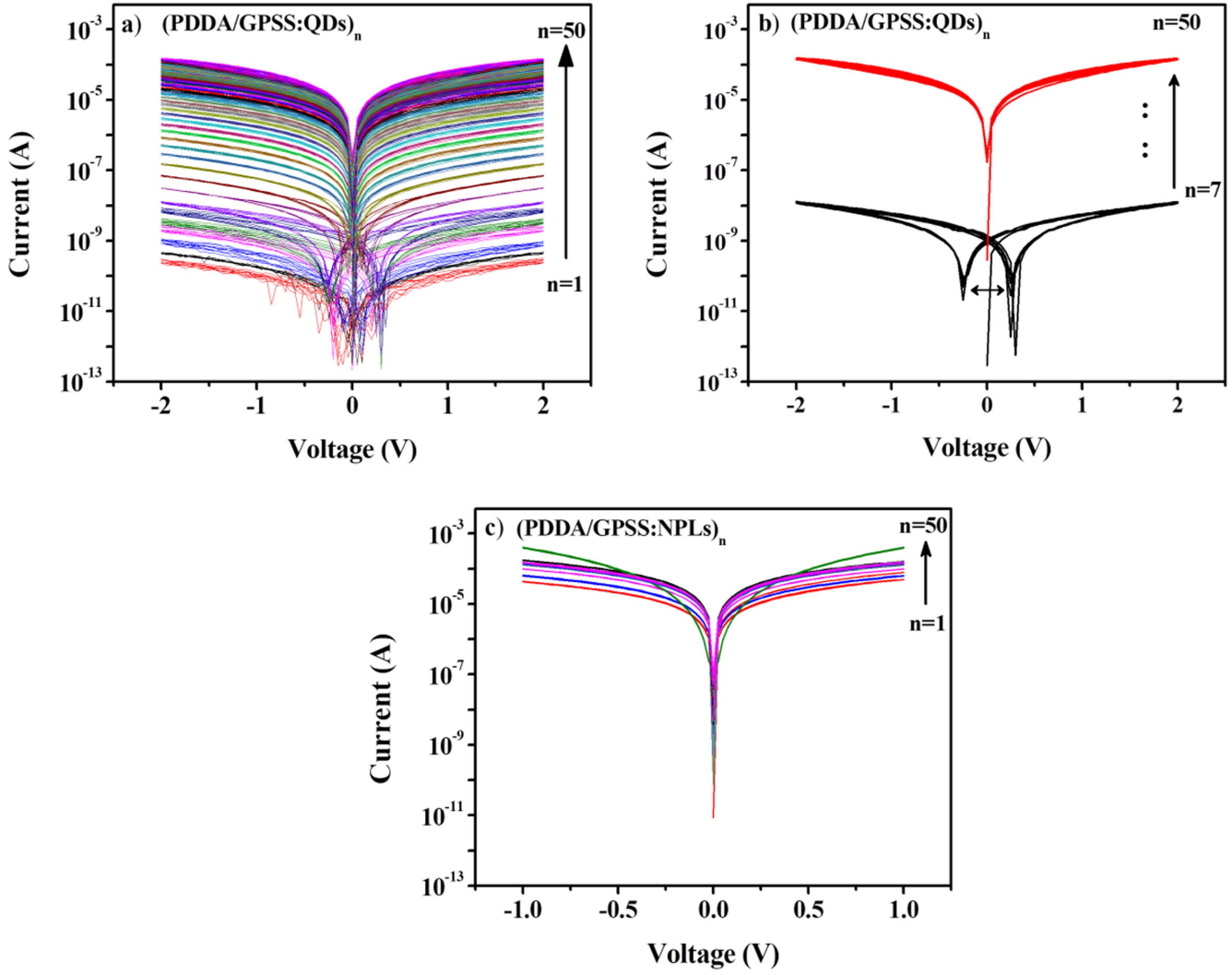


Figure 3. I - V measurements obtained in forward and backward sweeps during the LbL film growth: (a) (PDDA/GPSS:QDs)_{*n*}, for all n deposited layers, (b) details on the hysteresis for thin ($n < 10$) and thick ($n = 50$) (PDDA/GPSS:QDs)_{*n*} layers and (c) for all n deposited layers of (PDDA/GPSS:NPLs)_{*n*}.

transition potential, implying:

$$\mu_{\text{eff}} = \theta\mu = \frac{d^2}{\tau V_{\Omega}}, \quad (4)$$

$$n_0 = \frac{9 \varepsilon_r \varepsilon_0}{8 q \theta \mu \tau}. \quad (5)$$

Here, we found respectively $\mu_{\text{eff}} = 4.7 \text{ cm}^2 \text{ V}^{-1} \text{ s}^{-1}$ for GPSS:QDs and $\mu_{\text{eff}} = 34.7 \text{ cm}^2 \text{ V}^{-1} \text{ s}^{-1}$ for GPSS:NPLs, values superior to those early reported (10^{-2} – $1 \text{ cm}^2 \text{ V}^{-1} \text{ s}^{-1}$) and approach the very best mobility values found in the literature for rGO (43 – $188 \text{ cm}^2 \text{ V}^{-1} \text{ s}^{-1}$) [41]. The mobility values obtained from the SCLC calculations are also very close to those obtained from Hall effect measurements in the same LbL nanostructures (table 2), with negative values displayed for the bulk concentration confirming electrons as the majority carriers in both films. Our Hall coefficient (R_{H}) is relatively high ($\sim 10^4 \text{ cm}^3 \text{ C}^{-1}$) compared with the literature ($R_{\text{H}} \sim 0.02 \text{ cm}^3 \text{ C}^{-1}$) [41], but the interlocked multilayer structure formed with PDDA in the LbL films presented here result in lower conductivities due to the insulating nature of PDDA, which will be discussed in the sequence. At the same

time, the observed higher mobility and consequently higher R_{H} are related with conductive paths created inside the LbL layer containing rGO. In addition, impedance measurements associated with SCLC conduction is a simple alternative way to achieve reliable mobility values in LbL nanostructures.

The conductivities of both (PDDA/GPSS:QDs)_{*n*} and (PDDA/GPSS:NPLs)_{*n*} LbL films were calculated from the I - V curves in figure 3, and are illustrated in figure 5 as a function of the number of deposited bilayers.

The conductivity σ (dc) of the LbL films can be calculated using:

$$\sigma_{\text{dc}} = \frac{1}{RK_{\text{cell}}}. \quad (6)$$

R is the resistance of the film and K_{cell} is the cell constant [42] of the IDEs,

$$K_{\text{cell}} = \frac{N-1}{2}L \quad (7)$$

with N as the number of digits, L the length and w the width of each digit. Equation (7) is a simplified relationship valid only when $s = w$, where s is the distance between electrodes.

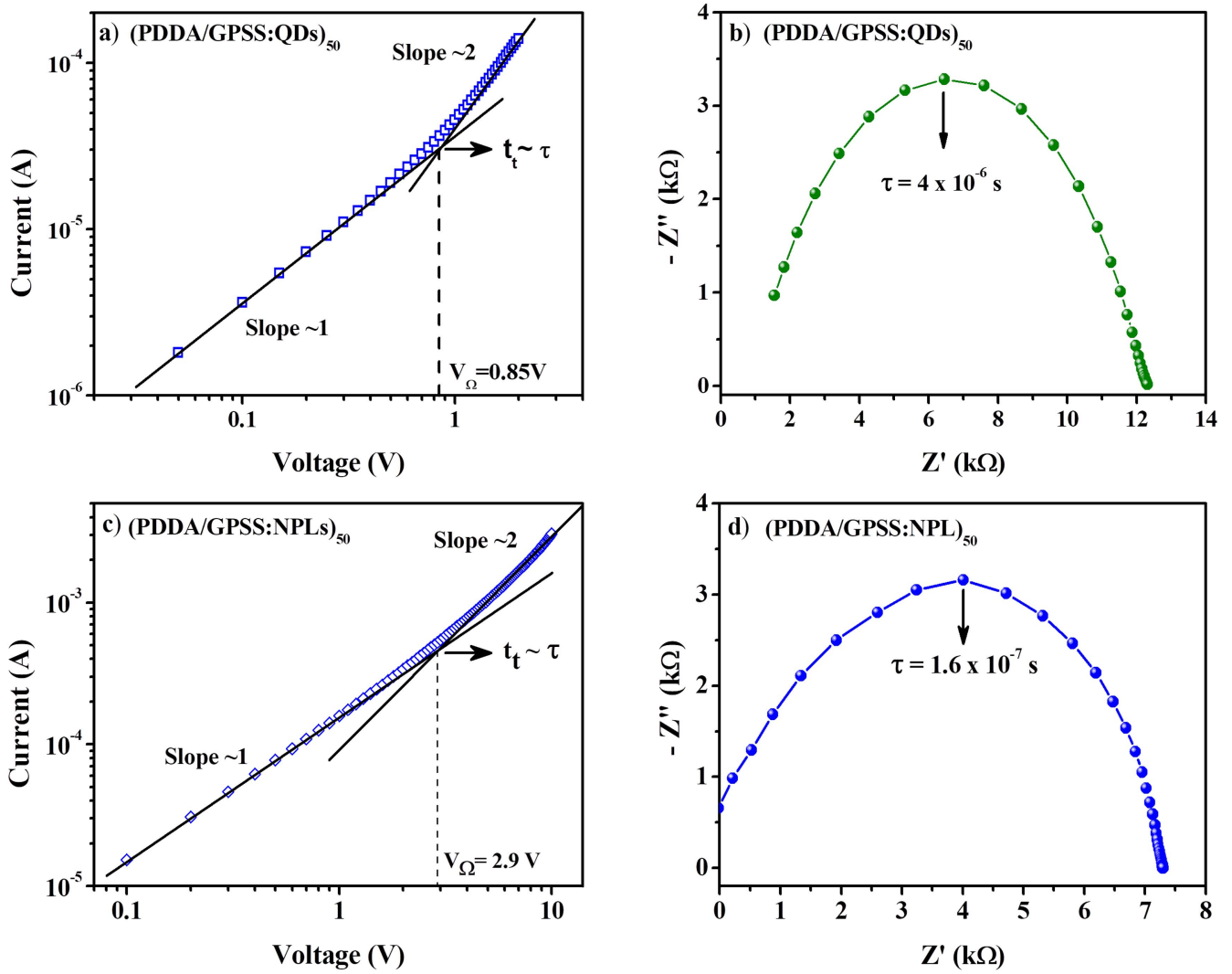


Figure 4. (a) I - V curve and (b) Nyquist plot for (PDDA/GPSS:QDs)₅₀; (c) I - V curve and (d) Nyquist plot for (PDDA/GPSS:NPLs)₅₀. V_{Ω} is the transition potential from ohmic to a second order ($I \propto V^2$) transport regime, t_t is the transit time of the carriers at V_{Ω} and τ is the dielectric relaxation time.

Table 1. Parameters obtained for the (PDDA/GPSS) LbL films considering the SCLC model and the ac electrical characteristics.

| LbL film | V_{Ω} (V) | τ (s) | n_0 (cm ⁻³) | $\mu_{\text{eff}} = \theta\mu$ (cm ² V ⁻¹ s ⁻¹) |
|--------------------------------|------------------|----------------------|---------------------------|---|
| (PDDA/GPSS:QDs) ₅₀ | 0.85 | 4.0×10^{-6} | 1.7×10^{13} | 4.7 |
| (PDDA/GPSS:NPLs) ₅₀ | 2.9 | 1.6×10^{-7} | 5.6×10^{13} | 34.7 |

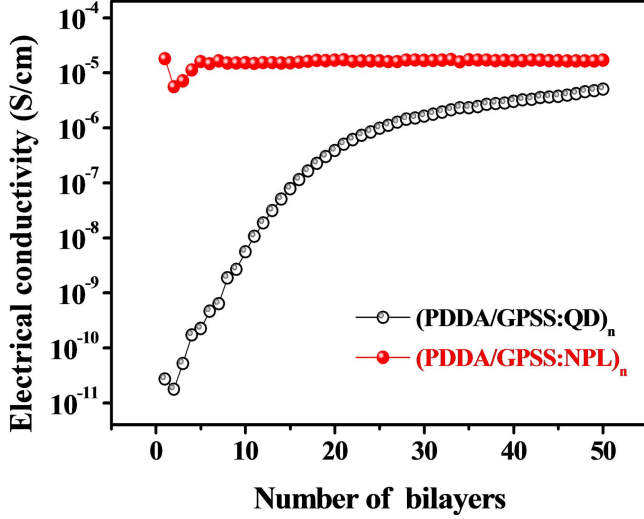
From figure 5 one can easily observe a strong dependence of σ_{dc} with the number of deposited layers for the (PDDA/GPSS:QDs) LbL films, while an almost constant σ_{dc} is achieved for the (PDDA/GPSS:NPLs) films right after the deposition of the 5th bilayer. This can be related to a faster coverage of the IDEs active area with the NPLs that have larger domains compared with the QDs, the later presenting also larger disordered regions as corroborated by the AFM analysis. Consequently, a larger number of GPSS:QDs layers are necessary to attain a constant conductivity value. The literature reports conductivities of $\sim 10^{-3}$ S cm⁻¹ for GPSS [43] and 0.2 S cm⁻¹ for LbL multilayered, polymer coated graphene composites [24]. It is worth mentioning that the

conductivity values reported here are low ($\sim 10^{-5}$ S cm⁻¹) due to the insulating PDDA layers interspersed between the conductive GPSS layers.

It is well known that chemically processed rGO presents structural defects and remaining OH groups [11], behaving similarly to disordered semiconductors where conduction by hopping plays a significant role. Thus, to evaluate the charge transport characteristics in defective LbL-based graphene structures, I - V measurements were performed varying the temperature (T) from 77 and 327 K, as illustrated in figures 6 and 7. The data was analyzed considering the VRH mechanisms such as Mott and Efros-Shklovskii (ES), with the main difference between them based on considerations of

Table 2. Parameters obtained for the (PDDA/GPSS) LbL films from Hall effect measurements.

| LbL film | μ_H (cm ² V ⁻¹ s ⁻¹) | Bulk concentration (cm ⁻³) | σ_H (S cm ⁻¹) |
|--------------------------------|--|--|----------------------------------|
| (PDDA/GPSS:QDs) ₅₀ | 4.5 ± 1.6 | (−5.6 ± 1.7) × 10 ¹³ | (7.4 ± 2.2) × 10 ⁻⁵ |
| (PDDA/GPSS:NPLs) ₅₀ | 21.5 ± 4.6 | (−8.4 ± 1.9) × 10 ¹³ | (2.8 ± 0.4) × 10 ⁻⁴ |

**Figure 5.** Electrical conductivity of (PDDA/GPSS)_n LbL films as a function of the number of deposited bilayers (*n*) for the QDs and NPLs structures.

the density of states (DOS) remaining constant or temperature-dependent, respectively. In general, in the ohmic regime the resistance (*R*) can be written as a function of temperature as [44, 45]:

$$R(T) = R_0 \exp\left(\frac{T_0}{T}\right)^p. \quad (8)$$

R_0 is a pre-exponential factor, T_0 a characteristic temperature of the distinct VRH models, and p defines the conducting model that better fits the experimental data. Mott considers a constant DOS as the temperature varies and shows $p = \frac{1}{(D+1)}$, where D is the dimensionality of the system. Consequently, for a Mott-VRH two dimensional system ($D = 2$), which is likely to be the case for graphene films, the characteristic temperature (T_M) is given by [45]:

$$T_0 \equiv T_M = \frac{3}{k_B N(E_F) \xi^2}, \quad (9)$$

where k_B is the Boltzmann constant, $N(E_F)$ is the DOS close to the Fermi level (E_F) and ξ is the localization length of the system. When an electron hops from an initial energy state to a final energy state, it leaves a hole in the initial state and creates an electron–hole interaction called as Coulomb gap, having energy E_{CG} . Efros and Shklovskii take into account the Coulomb interaction of the electron–hole pair and proposes that the DOS near the Fermi level is not constant and decreases with temperature, resulting in a dependence of R with the T described by equation (8), with $p = 1/2$ for any dimension. The characteristic temperature of the ES-VRH

driving mechanism (T_{ES}) is given by,

$$T_0 \equiv T_{ES} = \frac{2.8e^2}{4\pi\epsilon_r\epsilon_0 k_B \xi}. \quad (10)$$

In order to find the model that best fits our experimental data we must determine the p -value from equation (8), being also possible demonstrates that,

$$\frac{\partial \ln R(T)}{\partial \ln T} = -p \left(\frac{T_0}{T}\right)^p. \quad (11)$$

Defining $W \equiv -\frac{\partial \ln R(T)}{\partial \ln T}$, the p value can be obtained from the slope of the W versus T plot, as $\ln W = A - p \cdot \ln T$, where A is the linear coefficient of the curve [21].

Figures 6(a) and 7(a) show distinct I - V curves at different temperatures in the ohmic region for both (PDDA/GPSS:QDs)₅₀ and (PDDA/GPSS:NPLs)₅₀ films. Variations of the film electrical current with temperature confirm an activated transport mechanism. The respective film resistances at 50 mV decrease as the temperature increases, as shown in figures 6(b) and 7(b). For both LbL films, the best fitting (R -squared > 0.9) for the $\ln W$ versus $\ln T$ plot (figures 6(c) and 7(c)) was obtained considering the Mott-VRH mechanism, and the slope $p = 1/3$ suggests a 2D system characteristic of graphene [46]. A 3D system would be a good representation for the LbL films due to the interlocked multilayered nanostructure formed perpendicular to the plane of the substrate. However, considering the presence of insulating PDDA layers between conducting GPSS layers, the charge transport occurs preferably in the GPSS planes, thus resembling a 2D system.

The $\ln R$ versus $T^{-1/3}$ plots for (PDDA/GPSS:QDs)₅₀ and (PDDA/GPSS:NPLs)₅₀ LbL films (figures 6(d) and 7(d)) presented two different linear regimes, implying in two Mott characteristic temperature values for each film, as shown in table 3.

The literature points out that the hopping conductivity has constant activation energy (E_A) equivalent to a critical temperature value (T_c) where a transition occurs in the experimental data, here indicated by the arrow in figures 6(b) and 7(b) [47, 48]. Notice, at this region, there is a change in the trend of the resistance decay as the temperature increases for both studied films (figures 6(b) and 7(b)). From the $\ln R$ versus $T^{-1/3}$ plot (figures 6(d) and 7(d)), such a transition manifests as a change of the curve slope between the linear regimes observed, allowing us to experimentally determine T_c . Here, T_c values are respectively 247 K for NPLs and 237 K for QDs. For $T > T_c$ the activation energy is considered constant and can be obtained from an Arrhenius plot, obeying equation (12) [44]:

$$R = R_0 e^{\frac{E_A}{k_B T}}. \quad (12)$$

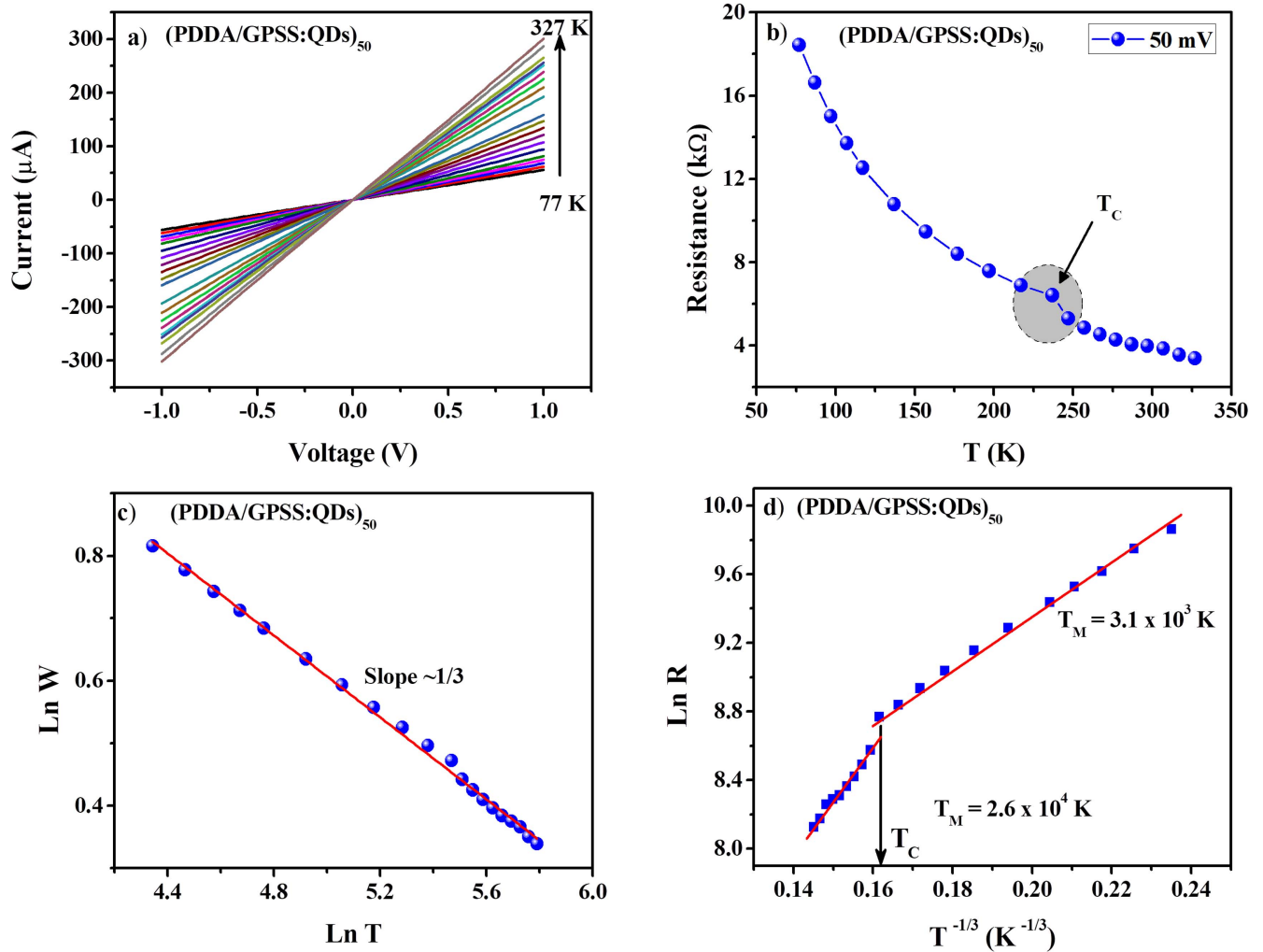


Figure 6. Temperature-dependent electrical characteristics of (PDDA/GPSS:QDs)₅₀ LbL films. (a) I - V curves, (b) R - T curves at 50 mV, (c) $\ln W$ versus $\ln T$ and (d) $\ln R$ versus $T^{-1/3}$.

It is worth mentioning that T_C is not exclusively related with the DOS near the Fermi level in the VRH models; that occurs whenever the DOS is concentrated in a finite interval close the Fermi level [44], as illustrated in figure 8 following an $\ln R$ versus T^{-1} dependence and also obeying Mott's law, as illustrated in figures 6(c) and 7(c). These also indicate that our experimental data fits well to the Mott's conduction mechanism having a 2D dimensionality over all temperature range (77 K–327 K) studied. Charge transport mechanisms usually follows equation (12) for $T > T_C$ when the charge carriers are thermally activated with a constant E_A , shown as an Arrhenius plot in figure 8. The E_A values found were, respectively, 68.9 meV for (PDDA/GPSS:NPLs)₅₀ and 36.5 meV for (PDDA/GPSS:QDs)₅₀.

At a first glance, a smaller activation energy associated with lower mobility value might seem contradictory for (PDDA/GPSS:QDs)₅₀, however, a quantum confinement of carriers in the QD domains [49] imply in higher relaxation dynamics (see figure 9). In addition, the large amount of QDs also favors a higher probability of random jumps between rGO conducting 'islands' distributed along with the GPSS: QDs plane layer, which contributes to a longer transit time of

the carriers and consequently lower mobility values. The opposite can be extended to the rGO NPLs case that requires higher E_A due to size and presence of defects, however, the NPLs display larger conductive pathways that on average result in higher mobilities, as observed here.

Conclusions

The multilayer films could be easily assembled with PDDA displaying a uniform material deposition during the LbL film fabrication, verified by UV-vis spectroscopy. AFM analysis indicated characteristic NPLs ranging in size from 0.5 to 1.5 μm with an average rms roughness of 1.2 nm, and QDs ranging from 20 to 65 nm and rms roughness of 6.4 nm. The film growth was also monitored by current-voltage I - V measurements that indicated a strong thickness-dependent response for the QDs, which attained conductivity values of $\sim 10^{-5}$ S cm⁻¹. For NPLs, right after the 5th bilayer the films attained constant and higher conductivities. Such behavior is intimately related to the type of GPSS nanostructure whereas NPLs possess larger sp^2 domains compared to QDs, favoring

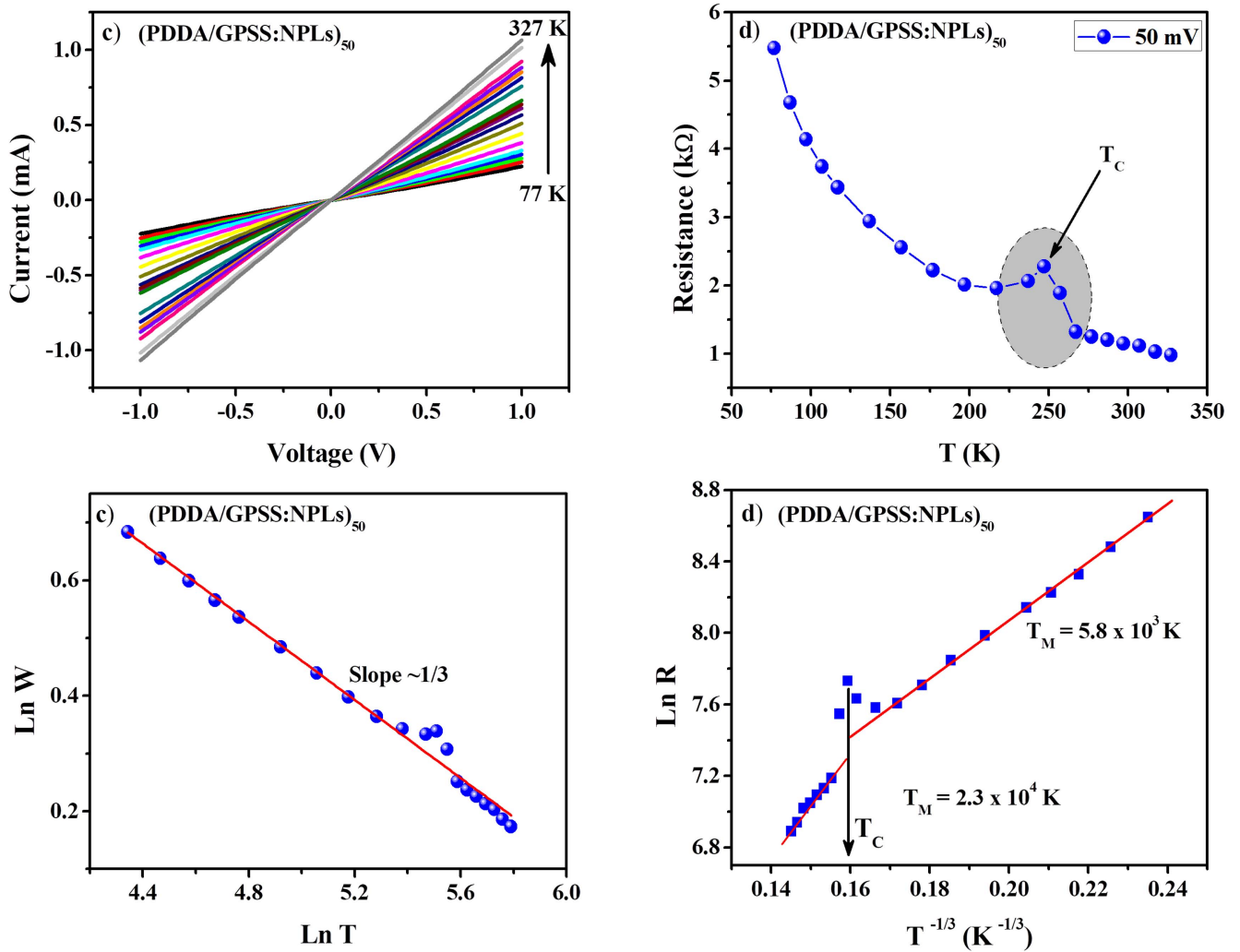


Figure 7. Temperature-dependent electrical characteristics of (PDDA/GPSS:NPLs)₅₀ LbL films. (a) *I*-*V* curves, (b) *R*-*T* curves at 50 mV, (c) *ln W* versus *ln T* and (d) *ln R* versus *T*^{-1/3}.

Table 3. Characteristic temperatures from the Mott-VRH model (*T_M*) for the LbL nanostructures.

| LbL film | <i>T_M</i> (K) | |
|--------------------------------|--------------------------|-----------------------|
| | 77 K → 237 K | 237 K → 327 K |
| (PDDA/GPSS:QDs) ₅₀ | 3.1 × 10 ³ | 2.6 × 10 ⁴ |
| (PDDA/GPSS:NPLs) ₅₀ | 5.8 × 10 ³ | 2.3 × 10 ⁴ |

the charge transport within the film. At low voltages, an ohmic regime in the *I*-*V* curves was identified for (PDDA/GPSS:QDs)_n and (PDDA/GPSS:NPLs)_n films, followed by a *I* ∝ *V*² dependence characteristic of the SCLC model in both cases. By combining SCLC data with electrical impedance results, it was also possible to calculate mobility values of 4.7 cm² V⁻¹ s⁻¹ for (PDDA/GPSS:QDs)₅₀ and 34.7 cm² V⁻¹ s⁻¹ for (PDDA/GPSS:NPLs)₅₀. These values were corroborated by Hall effect measurements and are among the average mobility reported for rGO structures. Temperature *I*-*V* measurements had shown a Mott-VRH mechanism and a 2D system

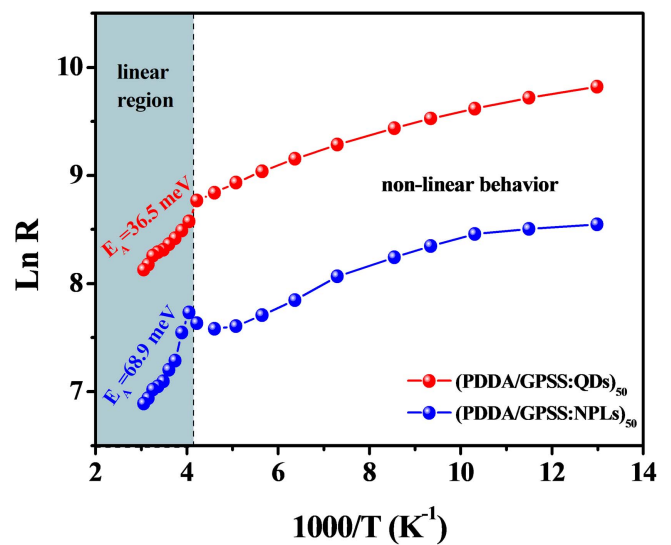


Figure 8. Arrhenius plots for (PDDA/GPSS)₅₀ LbL films either as QDs or NPLs. The linear region highlighted indicates thermally activated charge carriers, with the nonlinear part following Mott's law.

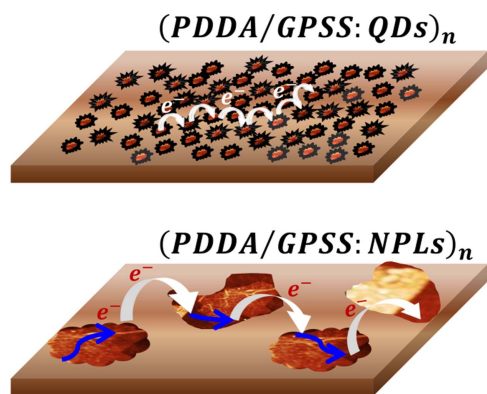


Figure 9. Sketch of transit of carriers in QDs and NPLs layers in the LbL structure. The white and blue arrows correspond, respectively, to inter and intra charge transport.

characteristic of graphene derivatives, with a 2D intra-planar conduction formed at the GPSS plane in the LbL assembly, with almost null inter-planar conduction between adjacent conductive layers due to the insulating nature of PDDA. Temperature measurements indicated higher probability of random jumps between rGO conducting ‘islands’ distributed along with the QDs layer, which contributes to a longer transit time of the carriers and consequently lower mobility values. On the opposite way, higher E_A were observed for rGO NPLs due to size and presence of defects, with larger conductive pathways that result in higher mobilities. Therefore, a better comprehension of the electron transport in rGO nanostructures can shine some light in future applications of hybrid, composite graphene-like materials with unique properties that can be synergistically explored with other conjugate materials.

Acknowledgments

Authors are grateful to FAPESP (2014/03691-7, 2014/25979-2), CNPq and CAPES for financial support.

ORCID iDs

Mawin J M Jimenez  <https://orcid.org/0000-0001-5666-6416>

Rafael F Oliveira  <https://orcid.org/0000-0001-8980-3587>

Marcelo A Pereira-da-Silva  <https://orcid.org/0000-0002-7197-4262>

Antonio Riul Jr  <https://orcid.org/0000-0002-9760-1851>

References

- [1] Lee C, Wei X, Kysar J W and Hone J 2008 Measurement of the elastic properties and intrinsic strength of monolayer graphene *Science* **321** 385–8
- [2] Castro Neto A H, Guinea F, Peres N M R, Novoselov K S and Geim A K 2009 The electronic properties of graphene *Rev. Mod. Phys.* **81** 109–62
- [3] Falkovsky L A 2008 Optical properties of graphene *J. Phys.: Conf. Ser.* **129** 12004
- [4] Grigorenko A N, Polini M and Novoselov K S 2012 Graphene plasmonics *Nat. Photon.* **6** 749
- [5] Singh V, Joung D, Zhai L, Das S, Khondaker S I and Seal S 2011 Graphene based materials: past, present and future *Prog. Mater. Sci.* **56** 1178–271
- [6] Kim H, Abdala A A and MacOsco C W 2010 Graphene/polymer nanocomposites *Macromolecules* **43** 6515–30
- [7] Jang J, Son M, Chung S, Kim K, Cho C, Lee B H and Ham M 2015 Low-temperature-grown continuous graphene films from benzene by chemical vapor deposition at ambient pressure *Sci. Rep.* **5** 1–7
- [8] Piccinini E, Bliem C, Reiner-Rozman C, Battaglini F, Azzaroni O and Knoll W 2017 Enzyme-polyelectrolyte multilayer assemblies on reduced graphene oxide field-effect transistors for biosensing applications *Biosens. Bioelectron.* **92** 661–7
- [9] Ponnamma D, Sadasivuni K K, Cabibihan J J, Yoon W J and Kumar B 2016 Reduced graphene oxide filled poly(dimethyl siloxane) based transparent stretchable, and touch-responsive sensors *Appl. Phys. Lett.* **108** 171906
- [10] Xu X, Huang D, Cao K, Wang M, Zakeeruddin S M and Grätzel M 2013 Electrochemically reduced graphene oxide multilayer films as efficient counter electrode for dye-sensitized solar cells *Sci. Rep.* **3** 1–7
- [11] Loh K P, Bao Q, Eda G and Chhowalla M 2010 Graphene oxide as a chemically tunable platform for optical applications *Nat. Chem.* **2** 1015–24
- [12] Sun S, Zhuang X, Wang L, Liu B, Zhang B and Chen Y 2017 BODIPY-based conjugated polymer covalently grafted reduced graphene oxide for flexible nonvolatile memory devices *Carbon* **116** 713–21
- [13] Tung T T, Robert C, Castro M, Feller J F, Kim T Y and Suh K S 2016 Enhancing the sensitivity of graphene/polyurethane nanocomposite flexible piezo-resistive pressure sensors with magnetite nano-spacers *Carbon* **108** 450–60
- [14] Tripathi K M, Kim T Y, Losic D and Tung T T 2016 Recent advances in engineered graphene and composites for detection of volatile organic compounds (VOCs) and non-invasive diseases diagnosis *Carbon* **110** 97–129
- [15] Alahbakhshi M, Fallahi A, Mohajerani E, Fathollahi M R, Taromi F A and Shahinpoor M 2017 High-performance Bi-stage process in reduction of graphene oxide for transparent conductive electrodes *Opt. Mater.* **64** 366–75
- [16] Ma W, Chen S, Yang S, Chen W, Weng W and Cheng Y 2017 Flexible all-solid-state asymmetric supercapacitor based on transition metal oxide nanorods/reduced graphene oxide hybrid fibers with high energy density *Carbon* **113** 151–8
- [17] Bahçeci Sertkol S, Esat B, Momchilov A A, Burak Yilmaz M and Sertkol M 2017 An anthraquinone-functionalized reduced graphene oxide as electrode material for rechargeable batteries *Carbon* **116** 154–66
- [18] Kajen R S, Chandrasekhar N, Pey K L, Vijila C, Jaiswal M, Saravanan S, Ng A M H, Wong C P and Loh K P 2013 Charge transport in lightly reduced graphene oxide: a transport energy perspective *J. Appl. Phys.* **113** 063710
- [19] Joung D, Chunder A, Zhai L and Khondaker S I 2010 Space charge limited conduction with exponential trap distribution in reduced graphene oxide sheets *Appl. Phys. Lett.* **97** 093105
- [20] Kumar R and Kaur A 2015 Charge transport mechanism of hydrazine hydrate reduced graphene oxide *IET Circuits, Devices Syst.* **9** 392–6
- [21] Chuang C, Puddy R K, Lin H D, Lo S T, Chen T M, Smith C G and Liang C T 2012 Experimental evidence for Efros–Shklovskii variable range hopping in hydrogenated graphene *Solid State Commun.* **152** 905–8
- [22] Kumar R, Dhawan S K, Singh H K and Kaur A 2016 Charge transport mechanism of thermally reduced graphene oxide

- and their fabrication for high performance shield against electromagnetic pollution *Mater. Chem. Phys.* **180** 413–21
- [23] Hummers W S and Offeman R E 1958 Preparation of graphitic oxide *J. Am. Chem. Soc.* **80** 1339
- [24] Rani A, Ah K, Koo H and Park M 2011 Multilayer films of cationic graphene-polyelectrolytes and anionic graphene-polyelectrolytes fabricated using layer-by-layer self-assembly *Appl. Surf. Sci.* **257** 4982–9
- [25] Marcano D C, Kosynkin D V, Berlin J M, Sinitskil A, Sun Z, Siesarev A, Alemany L B, Lu W and Tour J M 2010 Improved synthesis of graphene oxide *ACS Nano* **4** 4806–14
- [26] Gao K, Shao Z, Wu X, Wang X, Li J, Zhang Y, Wang W and Wang F 2013 Cellulose nanofibers/reduced graphene oxide flexible transparent conductive paper *Carbohydr. Polym.* **97** 243–51
- [27] Araki K, Wagner M J and Wrighton M S 1996 Layer-by-layer growth of electrostatically assembled multilayer porphyrin films *Langmuir* **12** 5393–8
- [28] Zheng Q and Kim J-K 2015 *Graphene for Transparent Conductors: Synthesis, Properties and Applications* (New York: Springer)
- [29] Prekodravac J R, Jovanovic S P, Holclajtner-Antunovic I D, Perusko D B, Pavlovic V B, Tosic D D, Todorovic-Markovic B M and Markovic Z M 2014 Monolayer graphene films through nickel catalyzed transformation of fullerol and graphene quantum dots: a Raman spectroscopy study *Phys. Scr. T* **2014** 014030
- [30] Dong Y, Shao J, Chen C, Li H, Wang R, Chi Y, Lin X and Chen G 2012 Blue luminescent graphene quantum dots and graphene oxide prepared by tuning the carbonization degree of citric acid *Carbon* **50** 4738–43
- [31] Luo P, Qiu Y, Guan X and Jiang L 2014 Regulation of photoluminescence properties of graphene quantum dots via hydrothermal treatment *Phys. Chem. Chem. Phys.* **16** 19011–6
- [32] Niu Z, Zhang L, Liu L, Zhu B, Dong H and Chen X 2013 All-solid-state flexible ultrathin micro-supercapacitors based on graphene *Adv. Mater.* **25** 4035–42
- [33] Negishi R, Akabori M, Ito T, Watanabe Y and Kobayashi Y 2016 Band-like transport in highly crystalline graphene films from defective graphene oxides *Sci. Rep.* **6** 28936
- [34] Lim E W and Ismail R 2015 Conduction mechanism of valence change resistive switching memory: a survey *Electronics* **4** 586–613
- [35] Chiu F 2014 A review on conduction mechanisms in dielectric films *Adv. Mater. Sci. Eng.* **2014** 1–18
- [36] Sleiman A, Mabrook M F, Nejm R R, Ayesh A, Al Ghaferi A, Petty M C and Zeze D A 2012 Organic bistable devices utilizing carbon nanotubes embedded in poly(methyl methacrylate) *J. Appl. Phys.* **112** 024509
- [37] Douvas A M, Makarona E, Glezos N, Argitis P, Mielczarski J A and Mielczarski E 2008 Polyoxometalate-based layered structures for charge transport control in molecular devices *ACS Nano* **2** 733–42
- [38] Chen W, Wang F, Qin S, Fang J, Wang C, Wang G, Wang L and Zhang X A 2015 Observation of complete space-charge-limited transport in metal-oxide-graphene heterostructure *Appl. Phys. Lett.* **106** 023122
- [39] Kao K C and Hwang W 1981 *Electrical Transport in Solids* (Oxford: Pergamon)
- [40] Chiu F-C, Chou H-W and Lee J Y 2005 Electrical conduction mechanisms of metal/La₂O₃/Si structure *J. Appl. Phys.* **97** 103503
- [41] Yang H, Cao Y, He J, Zhang Y, Jin B and Sun J 2017 Highly conductive free-standing reduced graphene oxide thin films for fast photoelectric devices *Carbon* **115** 561–70
- [42] Zacheja J and Binder J 1996 Fluid characterization using sensor elements based on interdigitated electrodes *Sens. Actuators B Chem.* **37** 37–42
- [43] Stankovich S, Dikin D A, Dommett G H B, Kohlhaas K M, Zimney E J, Stach E A, Piner R D, Nguyen S T and Ruoff R S 2006 Graphene-based composite materials *Nature* **442** 282–6
- [44] Shklovskii B I and Efros A L 1984 *Electronic Properties of Doped Semiconductors* (Berlin: Springer)
- [45] Joung D and Khondaker S I 2012 Efros–Shklovskii variable-range hopping in reduced graphene oxide sheets of varying carbon sp² fraction *Phys. Rev. B* **86** 1–8
- [46] Gómez-Navarro C, Weitz R T, Bittner A M, Scolari M, Mews A, Burghard M and Kern K 2007 Electronic transport properties of individual chemically reduced graphene oxide sheets *Nano Lett.* **7** 3499–503
- [47] Ansari M Z and Khare N 2015 Thermally activated band conduction and variable range hopping conduction in Cu₂ZnSnS₄ thin film *J. Appl. Phys.* **117** 25706
- [48] Vianelli A, Candini A, Treossi E, Palermo V and Affronte M 2015 Observation of different charge transport regimes and large magnetoresistance in graphene oxide layers *Carbon* **89** 188–96
- [49] Li L and Yan X 2010 Colloidal graphene quantum dots *J. Phys. Chem. Lett.* **1** 2572–6